RSC Advances

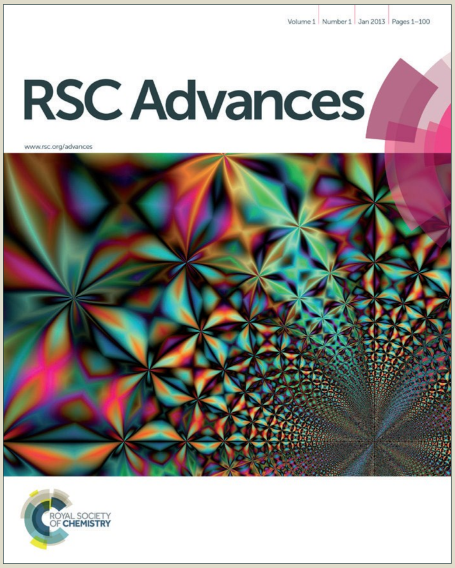

ROYAL SOCIETY OF CHEMISTRY

www.rsc.org/advances

Journal Name

ARTICLE

Structural, physical and chemical properties of nanostructured nickel-substituted ceria oxides under reducing and oxidizing conditions

Received 00th January 20xx,
Accepted 00th January 20xx

DOI: 10.1039/x0xx00000x

www.rsc.org/

R. O. Fuentes,[†,a,b] L. M. Acuña,[b,c] C. A. Albornoz,[a] A. G. Leyva,[a,d] N. Sousa[e] and F. M. Figueiredo[e]

This work reports the synthesis of nanostructured $Ce_{1-x}Ni_xO_{2-\delta}$ (x = 0.05, 0.1, 0.15 and 0.2) oxides prepared by cation complexation route and with the main objective of studying their redox properties using a combination of electron microscopy, synchrotron radiation X-ray diffraction (SR-XRD) and X-ray absorption near-edge spectroscopy (XANES). The $Ce_{1-x}Ni_xO_{2-\delta}$ series of nanopowders maintain the cubic crystal structure (Fm3m space group) of pure ceria, with an average crystallite size of 5-7 nm indicated by XRD patterns and confirmed by transmission electron microscopy. *In situ* SR-XRD and XANES carried out under reducing (5% H_2/He; 5% CO/He) and oxidizing (21%O_2/N_2) atmospheres at temperatures up to 500 °C show a Ni solubility limit close to 15 at.% in air at room temperature, decreasing to about 10 at.% after exposure to 5% H_2/He atmosphere at 500 °C. At room temperature in air, the effect of Ni on the lattice parameter of $Ce_{1-x}Ni_xO_{2-\delta}$ is negligible, whereas a marked expansion of the lattice is observed at 500 °C in reducing conditions. This is shown by XANES to be correlated with the reduction of up to 25% of Ce^{4+} cations to the much larger Ce^{3+}, possibly accompanied by the formation of oxygen vacancies. The redox ability of the Ce^{4+}/Ce^{3+} couple in nanocrystalline Ni-doped ceria is greatly enhanced in comparison to pure ceria or achieved by using other dopants (e.g. Gd, Tb or Pr), where it is limited to less than 5% of Ce cations.

INTRODUCTION

Cerium oxide (CeO_2, ceria) and ceria-based materials exhibit interesting physical and chemical properties, such as reversible surface oxygen ion exchange and electronic/ionic conductivity,[1,3] which are key for different applications, such as oxygen-conducting membranes for solid-oxide fuel cells (SOFC), the oxidation of carbon monoxide (CO) and hydrocarbon-based fuels (CH_4, C_4H_8, etc.), the water-gas shift reaction (WGS) and the production of hydrogen by the steam reforming of methanol.[4-7] Many studies have shown that the reducibility and catalytic activity of CeO_2 can be considerably enhanced by doping with small amounts of aliovalent transition metal cations.[8] Particularly for CeO_2–Ni cermet catalysts used for e.g. CO oxidation, NO reduction, methane combustion, and also as a functional coking-resistant SOFC anode,[9-12] the synergistic effect of Ni and CeO_2 with an enhanced O buffering effect of ceria by Ni-doping is thought to be crucial for the good catalytic performance. Nickel-doping has also been demonstrated to induce room-temperature ferromagnetism in ceria, forming a dilute magnetic semiconductor oxide.[13,14] The magnetic properties of doped-ceria appear as the perfect complement to the catalytic properties by enabling the magnetic recovery of ceria catalysts. Other applications such as e.g. magnetic storage or spintronic devices may also be envisaged.[15]

Cerium cations in the fluorite lattice can adopt mixed oxidation states Ce^{+4}/Ce^{+3}, whereas Ni tends to stabilize only as Ni^{2+}.[1] Moreover, Ni^{2+} in NiO is coordinated by 6 oxygen next nearest neighbors, but it can have up to 8 in the in a fluorite lattice (which is the coordination number of Ce).[16] Substantial structural perturbations of the ceria host lattice and a relatively low solubility limit for Ni are expected as result from the large difference between the ionic radii of Ce (${}^{VIII}r_{Ce}^{4+}$=0.97 Å, ${}^{VIII}r_{Ce}^{3+}$=1.14 Å) and Ni (${}^{VI}r_{Ni}^{2+}$=0.70 Å) cations.[17] Indeed, the Ni solubility in conventional micron-seized powders is less than 1 at.%.[3] In nanoparticles, however, Ni has been found to be soluble up to 20 at.% in $Ce_{1-x}Ni_xO_{2-y}$ obtained by a sol-gel route

---

[a] Departamento de Física, Centro Atómico Constituyentes, CNEA, Av. Gral. Paz 1499, (1650) San Martín, Buenos Aires, Argentina.
[b] CONICET, Buenos Aires, Argentina.
[c] CINSO (Centro de Investigaciones en Sólidos), CONICET-CITEDEF, J.B. de La Salle 4397, 1603 Villa Martelli, Buenos Aires, Argentina.
[d] Escuela de Ciencia y Tecnología, Universidad Nacional de San Martín, M de Yrigoyen3100, (1650) San Martín, Buenos Aires, Argentina.
[e] Department of Materials and Ceramic Engineering, CICECO, University of Aveiro, 3810-193 Aveiro, Portugal.
† Corresponding author: rofuentes@conicet.gov.ar. Phone: +5411 6772 7111

Electronic Supplementary Information (ESI) available: SR-XRD patterns recorded at 500 °C in different atmospheric conditions for nanostructured CeNi are exhibited in Fig. S1–S3 and their corresponding structural parameters and standard Rietveld agreement factors are presented in Tables S1–S3, nitrogen adsorption isotherms of the as-prepared and calcined nanopowders are exhibited in Fig. 4 and the Ce L3-edge XANES spectra and their corresponding fits of the nanostructured CeNi at 500 °C under different atmospheric conditions are shown in Fig. S5–S7, and finally, the fraction of Ce present as Ce^{3+} in nanostructured CeNi05, CeNi10 and CeNi20 powders under reducing and oxidizing conditions at 500 °C are presented in Table S4. See DOI: 10.1039/x0xx00000x (crystallite size 5-9 nm).[13] Lower values of 10 to 12 Ni at.% were found for similarly sized nanopowders (~7 nm) prepared by a reverse micro-emulsion method, with metallic Ni being formed for $x \geq 0.15$.[18] An even lower solubility limit, between 8 and 10 at.%, was reported for nanopowders obtained by the thermal decomposition of oleate metal organic precursors (crystallite size also ~7 nm).[14]

Barrio *et al*. report a detailed XRD study describing a fluorite type structure containing ordered Ni-O-Ni entities where the Ni^{2+} cations are reduced (in hydrogen atmosphere) at 400-700 °C, while the reduction of Ce^{4+} to Ce^{3+} is apparent as an expansion of the lattice above 700 °C.[18] Interface interactions Ni↔O↔Ce are suggested to explain the enhanced redox stability of Ni in the fluorite lattice (NiO will reduce at 300 °C). However, the knowledge about these interactions and the evolution of the Ce oxidation state in the presence of Ni has not been characterized, which is important for a better understanding of the catalytic and electro catalytic processes on the these materials.

In the present work, nanostructured $Ce_{1-x}Ni_xO_{2-\delta}$ (x = 0.05, 0.1, 0.15 and 0.2) oxides were synthesized by a cation complexation method with the main objective of studying their redox properties using a combination of synchrotron radiation X-ray diffraction (SR-XRD) and X-ray absorption near-edge spectroscopy (XANES) carried out *in situ* under reducing (5% H_2/He; 5% CO/He) and oxidizing (21%O_2/N_2) atmospheres at temperatures up to 500 °C. A detailed structural and microstructural *post mortem* characterization of these materials by scanning and high resolution transmission electron microscopy (SEM and HRTEM) and energy dispersive X-ray spectroscopy (EDS) is also provided.

EXPERIMENTAL

Nickel-doped ceria nanopowders were synthesized by the cation complexation method previously reported by the authors to obtain nanostructured ceria based oxides.[19] $Ce(NO_3)_3.6H_2O$ (99.99%, Alfa Aesar) and $Ni(NO_3)_3.6H_2O$ (99.9%, Alfa Aesar) were employed as precursors. Each nitrate was dissolved in d.i. H_2O separately and then the solutions were mixed to obtain nitrate solutions with molar ratios of Ce:Ni appropriate for the preparation of $Ce_{0.95}Ni_{0.05}O_{2-\delta}$ (CeNi05), $Ce_{0.9}Ni_{0.1}O_{2-\delta}$ (CeNi10), $Ce_{0.85}Ni_{0.15}O_{2-\delta}$ (CeNi15) and $Ce_{0.8}Ni_{0.2}O_{2-\delta}$ (CeNi20) samples. Citric acid (99.5%, Merck) was dissolved in deionized water and this was added to the cation nitrate solution in appropriate amounts to give a molar ratio of final total oxide to citric acid of 1:2. After homogenization, the solution was heated to 100 °C and maintained under stirring to remove excess water and NO_2, and to convert it to a transparent gel. While raising the temperature, the solution became more viscous with evolution of foam, and finally it gelled without any visible precipitation or turbidity. The drying was completed by placing the gel in a muffle at 100 °C for 20 min. The initial thermal decomposition of the precursor was carried out at 250 °C for 1 h in air and the resulting ash-like material was calcined at 500°C for 1 h, also in air. The same method was employed to obtain pure CeO_2, here used as reference sample.

Thermal analysis (TG/DTA) of the gel precursors of CeNi was carried out in flowing air with a heating rate of 10 °C.min^{-1} up to 800 ◦C in an Al_2O_3 crucible using a ShimadzuDTG-50 apparatus.

The as-prepared and annealed powders were carefully ground in an agate mortar for at least 15 minutes for subsequent analysis by electron microcopy and -196 °C nitrogen sorption isotherms. For the microscopy observations, a small amount of the milled powder was dispersed in dry n-hexane (Sigma-Aldrich, PA). Carbon/carbon film copper grids (Agar Scientific) were dipped in those suspensions and let dry at open air covered from dust. The powders without any further modification were firstly observed by scanning electron microscopy (SEM) and low resolution scanning transmission microscopy (STEM) on a Hitachi SU-70 microscope operating at respectively 15 and 30 kV, which also allowed elemental analysis using aBrukerQuantax400 energy dispersive spectroscopy (EDS) detector. The same grids were subsequently analyzed in high resolution TEM on a Jeol 2200 microscope operating at 200 kV, which was also operated in STEM mode mainly for EDS elemental analysis using an Oxford INCA Energy TEM 250 detector.

The nitrogen N_2 sorption isotherms were collected on a Micromeritics Gemini system. The samples were previously degassed overnight at 200 °C and the isotherms were collected at -196 °C. The specific surface area, S_{BET}, was estimated by the BET method and the pore size distribution by the BJH method.

In order to verify the phase composition, conventional X-ray diffraction (XRD) was performed in a PANalytical Empyream2 with a PIXcell^{3D} detector employing Cu-K_α radiation (of wavelength 1.5418 Å). Data in the angular range 2θ = 20 - 90° were collected in step-scanning mode, with a step length of 0.04° and a step-counting time of 4 s.

XRD patterns were recorded at 500 °C and in controlled atmospheres using synchrotron radiation at the D10B-XPD beamline of the National Synchrotron Light Laboratory (LNLS, Campinas, Brazil). In these *in situ* XRD experiments, the sample was mounted on a ceramic sample-holder and placed in a furnace. The X-ray wavelength was set at 1.55033 Å. Data in the angular range 2θ = 20 - 85° were collected in step-scanning mode, with a step length of 0.05° and a step-counting time of 4 s. The data were collected at temperatures room temperature and at 500 °C. The sample was heated at a rate of 10 °C.min^{-1}, and a soak time of 10 min was employed before performing the XRD scan at 500 °C in different atmospheres. The thermal and redox behavior of the materials was studied in 5% H_2/He (20 ml.min^{-1}), in dry synthetic air (50 ml.min^{-1}) and in 5% CO/He (20 ml.min^{-1}), in this order. NIST SRM 640c Si powder was used as the standard for the instrumental broadening correction.

A crystallographic study to obtain the lattice parameters and the phase composition was performed by Rietveld refinement of the X-ray diffraction data employing the FullProf suite of software.[20] For Ni-doped ceria oxides, the cubic phase of pure CeO_2 described in ICDS#24696 (Fm3m space group) was assumed with the Ni^{2+} and Ce^{4+}cations in 4a position, and O^{2-} anions in the 8c positions. Depending on the atmospheric conditions, a segregated secondary phase of NiO was assumed in oxidizing conditions (space group Fm3m with Ni^{2+} and O^{2-} in 4a and 4b positions, according to ICDS#182984), and Ni assumed in reducing conditions (space group Fm3m with Ni in 4a position, according to ICDS#162279). The peak shape was described by a pseudo-Voigt function. The background of each profile was fitted using a six-parameter polynomial function in $(2\theta)^n$, n = 0–5. The thermal parameters were assumed to be equal. The quality of the refinements was monitored by reliability indices. These indices are weighted R (R_{wp}), the reduced chi-squared (χ^2), and R_e, which are related just to the profile of the XRD patterns, and R_p, which is related to the crystal structure. The reduced chi-squared is defined as $(R_{wp}/R_e)^2$, where R_{wp} is the index that should be analyzed to verify if the refinement is converging and R_e is the expected statistical value for R_{wp}.[21] The average crystallite size was obtained using the Scherrer formula from the extent of peak broadening of the main XRD reflection (111).[22] Errors in crystallite size were derived by estimating the error in the FWHM (full-width at half-maximum) to be equal to the 2θ step.

In situ X-ray absorption near-edge spectroscopy (XANES) experiments under conditions of controlled temperature and atmosphere were carried out at the D04B-XAFS1 beamline at LNLS in transmission mode using a Si(111) monochromator for the Ce L_3-edge (5726 eV) and Ni K-edge (8333 eV). The nominal photon flux of the beamline is $3x10^9$ photons/(s.mrad.100mA) @ 6 keV. All spectra were collected at energies in the range 5690-6100 eV (for the Ce L_3-edge) and 8283-8700 eV (for the Ni K-edge) with E/ΔE=5000 to 10000 in both cases. Energies for the Ce L_3-edge and Ni K-edge were calibrated using Cr (5989 eV) and Ni (8333 eV) foils, respectively. Two acquisitions were made on the same sample to improve the signal to noise ratio. Samples were diluted with boron nitride and these mixtures were pressed into 15 mm diameter pellets (around 6 mg of sample and 70 mg of diluent were used). For the transmission measurements, the pellets were placed in a tubular quartz furnace (diameter, 20 mm; X-ray path length, 440 mm) sealed with refrigerated Kapton windows. Temperature was measured and controlled by a thermocouple passed down the sample holder and positioned close to the surface of the pellet. Temperature-resolved XAS spectra at the Ce L_3-edge and Ni K-edge were acquired during temperature programmed reduction under 5% H_2/He (20 ml.min^{-1}) at temperatures from 25 to 500 °C at a heating rate of 10 °C.min^{-1} and with a total data acquisition time of 20 min per spectrum. After the data were collected at 500 °C under 5% H_2/He, the system was purged with N_2 (100 ml.min^{-1}) and synthetic air (50 ml.min^{-1}) was passed through the furnace. After 10 min, data were collected under these oxidizing conditions. Finally, the system was purged with N_2 (100 ml.min^{-1}) and 5% CO/He (50 ml.min^{-1}) was passed through the cell and after 10 min, data were collected.

RESULTS AND DISCUSSION

Thermal behavior and room temperature structural characterization

The thermal behavior of the gel precursors was very similar for all samples. **Figure 1** shows the TG/DTA plot obtained in air for CeNi20 as a typical example. The DTA curve exhibits a weak endothermic peak at 115 °C (starting at 95 °C) followed by one exothermic peak at 140 °C. This endothermic-exothermic sequence can be ascribed to the polymerization reactions accompanying gel formation, where the Ce and Ni complex cations are increasingly cross linked by the progressive substitution of water ligands by the tridentate citrate ion. The initial activation of the process should consume some energy to trigger the water release and hence the initial endothermic peak. However, since the –COO– groups would be expected to bond more strongly than water to the metal centers and since the formation of a gel from a solution would cause an increase in entropy, this process is expected to be exothermic. This first set of DTA events is accompanied by a very sharp weight loss of 30% up to 160 °C. The TGA curve displays a second weigh loss stage of about 15% between approximately 160 °C and 250 °C, which seems to correspond to a couple of extremely weak endothermic phenomena (at 180 °C and 225 °C), most likely due to solvent release and small structural rearrangements. There is a third weight loss of ~20% spanning from 270 °C to 330 °C which is clearly associated to the most intense endothermic peak in the DTA curve (starting at 245 °C and reaching a maximum at 330 °C). These events can be related to the burn out of organic materials, by liberation of NO_x, CO, CO_2, and to the crystallization of the CeNi20 solid solution, as observed for other ceria-based powders prepared by the same route.[23-25] Above 350 °C the material is stable, without any further thermal or weight changes up to 800 °C.

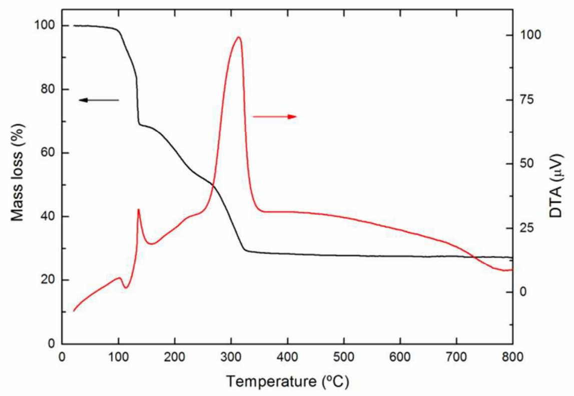

Figure 1. TG/DTA of metal nitrate precursor mixtures corresponding to cation complexation method for CeNi20.

In **Figure 2a**, SR-XRD patterns recorded in air with their Rietveld refinement are exhibited for the obtained CeO_2 and Ni-doped ceria oxides. The zoomed area in **Figure 2b** shows a hint of the of NiO diffraction maxima on the pattern of the

CeNi15, and clearly visible peaks for CeNi20.The patterns of the other three phases are those of a single fluorite phase such $CeO_{2,}$. Calculations by Rietveld refinements (**Table 1)** yield about 4%NiO for CeNi15 and CeNi20, and still a residual amount for CeNi10. Despite the associated errors, these values indicate a solubility limit of Ni in CeO_2 placed closer to the lower limit of the compositional interval between 10 and 15 at.% Ni, in very good agreement with values found for powders obtained by other synthetic methods and fired at temperatures close to 450-500 °C.[18]

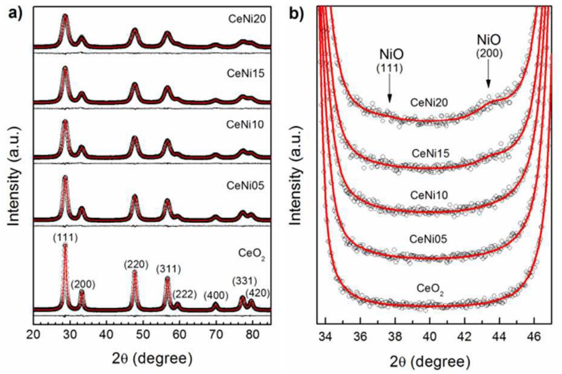

Figure 2. Synchrotron XRD patterns recorded at room temperature (empty circles) with the Rietveld-fitted pattern (red line) and the difference plot for nanostructured nickel-doped ceria oxides with different Ni content: a) whole pattern and b) zoom (arrows are pointed out NiO phase segregation).

Table 1. Structural parameters, phase composition and standard Rietveld agreement factors for pure ceria and Ni-substituted ceria at room temperature in air.

Sample	CeO_2	CeNi05	CeNi10	CeNi15	CeNi20
a (Å)	5.4144(6)	5.4150(6)	5.4149(6)	5.4163(3)	5.4173(2)
V (Å^3)	158.733(3)	158.784(3)	158.772(4)	158.896(7)	158.983(1)
R_p	3.19	3.60	3.90	4.20	4.20
R_{wp}	4.85	4.96	5.34	5.72	5.77
R_e	4.50	4.56	4.63	4.71	4.69
χ^2	1.16	1.19	1.33	1.48	1.51
%(Ce,Ni)O$_2$ phase	-	100	100	98(1)	96(1)
%NiO phase	-	0	0	2(1)	4(1)

The evolution of the room temperature lattice parameter with the Ni content does not depict a clear trend and in absolute values they are rather weak. If on the one hand the unit cell volume of all CeNi nanopowders is slightly larger than for pure ceria (5.4144 Å), on the other hand the dependence with composition clearly deviates from a Vegard's law, even within the single phase range (up to 10 at.% Ni). Due to the smaller ionic radiius of Ni^{2+}(0.70 Å) than that of Ce^{4+}(0.97 Å), one expects that substitution of Ni into ceria leads to a lattice contraction. Ce can adopt formal oxidation states Ce^{+4} or Ce^{+3} which, contrary to the Ni^{2+}, is much larger than Ce^{4+} (1.14 Å *vs.* 0.97 Å), hence leading to lattice expansion. Oxygen vacancies are likely to form in both situations in order to maintain charge balance resulting from the substitution of C^{4+} by lower valent Ce^{3+} or Ni^{2+}.[3,13,18,26,27] The literature is conflictive in this regard, reporting both lattice expansion[18] and contraction[13] effects. In the present case, the observed slight lattice expansion in the room temperature patterns indicates a dominating effect of the oxygen vacancies, which is preferentially kinked to the dopant Ni^{2+} cations. The partial $C^{4+} \rightarrow Ce^{3+}$ reduction, as shown in another section of this paper, is unlikely in face of the very minor effect at room temperature and in oxidizing conditions. We show in the following section that the situation is totally different at high temperature and in reducing environment.

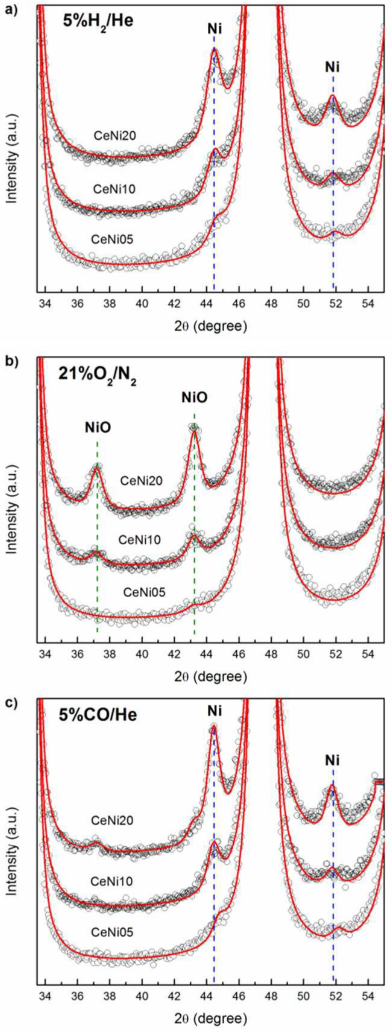

Figure 3. Synchrotron XRD patterns for nanostructured CeNi (empty circles) with the Rietveld-fitted pattern (red line) recorded at 500ºC in sequential atmospheres of a) 5% H_2/He, b) 21% O_2/N_2 and c) 5% CO/He.

In situ high-temperature characterization

The structural studies were also performed *in situ* at 500 °C under different gas conditions starting with a reducing treatment in 5% H_2/He, a reoxidation in 21% O_2/N_2 and again a reducing atmosphere consisting of 5% CO/He. The obtained SR-XRD patterns and corresponding Rietveld refinement results are show in Supporting Information (**Figures S1-S3 and Tables S1-S3**).

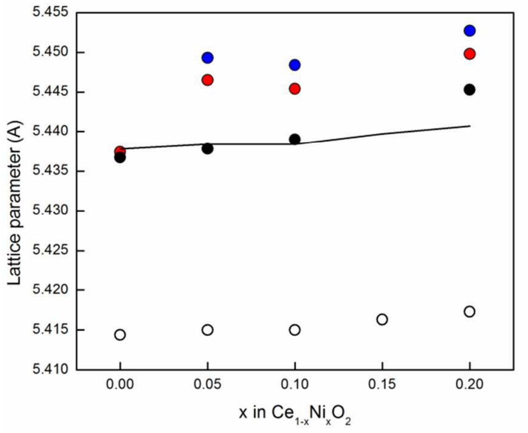

Figure 4. Lattice parameters obtained by Rietveld refinements of SR-XRD patterns collected at room temperature (empty circles) and at 500ºC under a sequence of atmospheres corresponding to 5% $_{H2}$/He (red circles), 21% O_2/N_2 (black circles) and 5% CO/He (blue circles). Solid line corresponds to lattice parameters obtained by reported thermal expansion coefficient for pure ceria.[28]

Figure 4 compares the lattice parameters of the various CeO_2 and CeNi powders measured at room temperature with those obtained at 500 °C. The small lattice expansion at room temperature in air observed with increasing Ni content is reproduced at 500 °C, despite the obvious effect of the thermal expansion (the solid line in **Figure 4** is a prediction based on reported thermal expansion coefficient for pure ceria, 9 to 10×10^{-6} K^{-1}).[28] Any chemical expansion is negligible, considering the virtually identical values obtained for CeO_2 in air and hydrogen at 500 °C, thus confirming the expected redox stability of CeO_2 in this temperature and oxygen partial pressure range.[3] This means that the effect is most likely due to the formation of oxygen vacancies to compensate for the positive charges associated to the dopant nickel cations $Ni_{Ce}^{\cdot\cdot}$ (here noted in Kroger Vink notation), which, as found for the patterns collected in air at room temperature, prevails over the lattice contraction caused by the smaller Ni^{2+} cations effectively solubilized in the ceria lattice. However, samples containing Ni first exposed to the H_2 expand more than pure ceria. This can be explained invoking the increase of the fraction of the larger Ce^{3+} cations favored by the reducing H_2 atmosphere (this is indeed the case as shown elsewhere). On switching to oxidizing conditions (synthetic air) at 500 °C, the lattice parameters were seen to decrease for all samples, but to different extents (**Figure 4**, black circles). The difference increases with decreasing Ni content may be a further indication that of the effect of the Ce^{4+}/Ce^{3+} redox couple as the main cause of the observed structural changes. On switching again to reducing conditions (5%CO/%He, blue circles), the lattice parameters increase again achieving values slightly higher than those obtained in 5%H_2/He but retaining the exact same compositional trend. These differences may result from Ni segregation from CeO_2 during the high temperature treatment in hydrogen.

Microstructural characterization

The as-prepared powders appear on SEM micrographs (**Figure 5A and 5C**) in the form of aggregates shaping a foam-like microstructure of spherical pores with a bi-modal size distribution, one centered around 0.5-1 µm, and another, much smaller, close to 100 nm. Images collected at higher magnification reveal clearly nanometric powders, which TEM will confirm of size smaller than 10 nm. These characteristics were maintained after firing at 500 °C in hydrogen.

Table 2. Crystallite average size (D_{XRD}), specific surface area (S_{BET}) and calculated primary particle size (d_{BET}) for the as-prepared CeNi powders and after firing at 500 °C in 10% H_2/N_2.

	As-prepared				After 500 °C in 10% H_2/N_2			
Sample	D_{XRD}/nm	D_{TEM}/nm	$S_{BET}/m^2.g^{-1}$	d_{BET}/nm	D_{XRD}/nm	D_{TEM}/nm	$S_{BET}/m^2.g^{-1}$	d_{BET}/nm
CeO_2	11.9	-	26	35	14.7	-	-	-
CeNi05	7.1	-	39	22	10	-	26	33
CeNi10	5.9	5.3±1.0	37	24	10	7.9±2.4	34	26
CeNi15	5.6	-	31	29	-	-	17	53
CeNi20	5.0	5.9±0.9	35	26	9.8	8.8±2.0	26	35

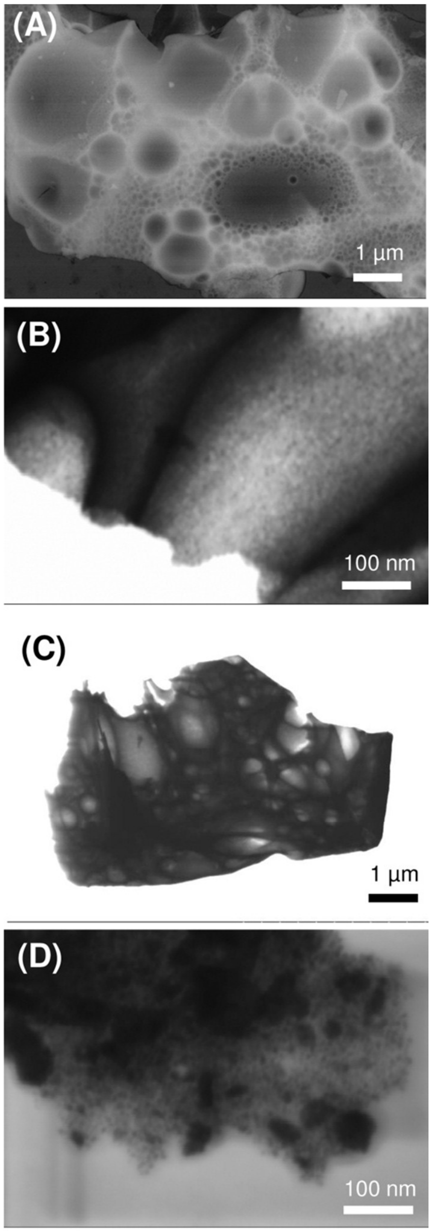

Figure 5. Low resolution STEM micrographs of (A,B) CeNi10 and (C,D) CeNi20 collected on the as prepared powders.

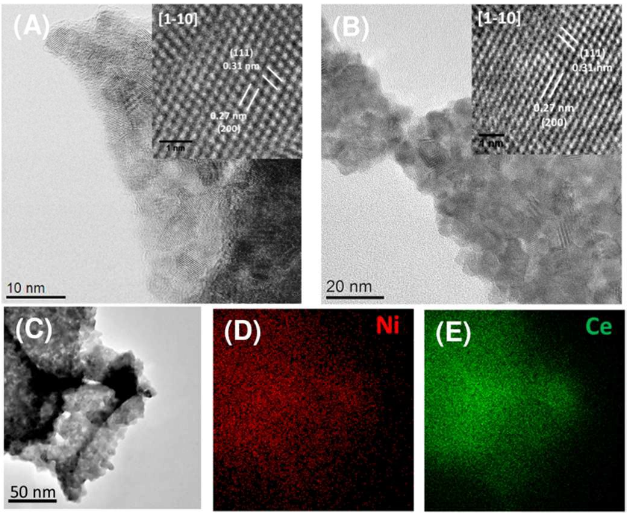

Figure 6. HRTEM micrographs of CeNi10 collected on (A) as-prepared powders and (B, C) after annealing at 500 °C under a 5%H_2/N_2 gas flow. Note the slight crystallite size from 5 nm to 8 nm upon annealing. (D) and (E) are Ni and Ce elemental distribution maps obtained by EDS in region in (C) confirming the homogeneous distribution of Ni.

Somewhat lower S_{BET} values are found for the samples annealed at 500 °C in hydrogen, suggesting a slightly higher degree of agglomeration as result of redox cycle imposed to the material. The primary particle size estimated from S_{BET} assuming spherical particles (d_{BET}) is in the range of 22-29 nm for the fresh samples, and slightly higher (26-53 nm) after the reducing treatment, reflecting the lower S_{BET}. Comparison with the pure CeO_2 reference suggests a limiting role of Ni on the size of primary particles. These particles are aggregates of crystallites with an average size (D_{XRD}) of 12 nm for pure CeO_2 down to just 5 nm for the most substituted composition CeNi20, according to estimates obtained from the powder XRD patterns, also listed in **Table 2**. The crystallite size of the Ni-containing powders increases after firing at 500 °C in hydrogen (D_{XRD}≈10 nm), regardless of the Ni content.

The TEM images shown in panels (A) and (B) of **Figures 6** and **7** show agglomerates of highly crystalline nanoparticles with size of 5-6 nm for the as-prepared powders, and 8-9 nm for those fired at 500 °C in reducing conditions, confirming on the local scale the results obtained from the XRD patterns. No evidence for Ni segregation could be found on any of the sampled particles of CeNi10, with EDS maps obtained in STEM mode revealing a homogenous distribution of Ni and Ce in both fresh and reduced powders (**Figure 6C-6E**). Some free Ni-containing phase is to be expected in CeNi10 according to XRD, but the intensity of the reflections is extremely low (**Figure 3a**), thus indicating that the amount of such phase may be statistically difficult to detect by a local sampling technique such as TEM. Nevertheless, XRD indicated a much larger amount of Ni for CeNi20 and indeed the presence of segregated Ni particles was easily observed on the reduced samples, as illustrated by **Figure 7C-7G**.

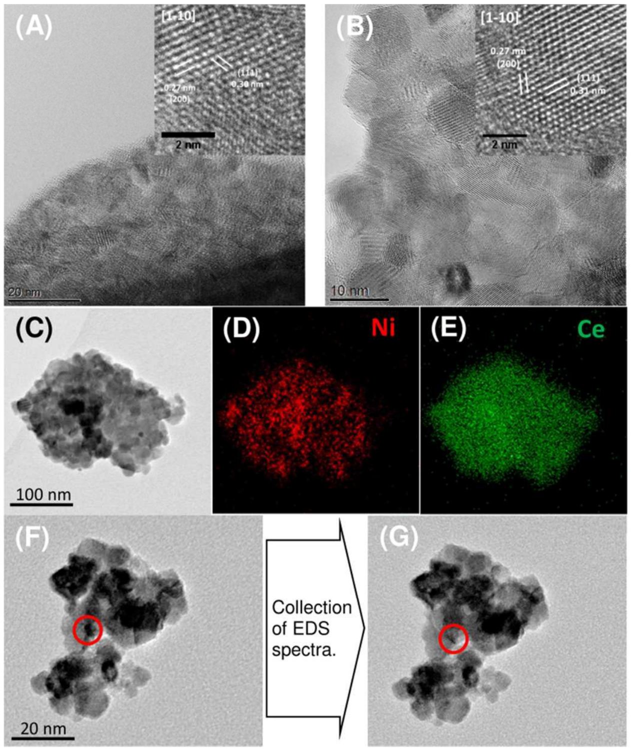

Figure 7. High resolution TEM micrographs of CeNi20 collected on (A) as-prepared powders and (B, C) after annealing at 500 °C under a 5% H_2/N_2 gas flow. Besides the noticeable increase of the crystallite size from ⍰6 nm to ⍰9 upon annealing, (D) and (E) EDS elemental maps show the existence of Ni-rich regions appearing as dark spots in STEM images (C). These Ni-rich crystallites were unstable under the electron beam, with Ni diffusing away after a couple of minutes of beam incidence for collecting EDS spectra, as shown by comparison of the circled regions in (F) and (G).

In situ XANES studies under variable temperature and atmosphere

Normalized Ce L_3-edge XANES spectra for nanostructured CeNi powders obtained at different temperatures and different atmospheres are exhibited in **Figure 8 a, b and c**. Major differences are due to the surrounding atmosphere, with the spectra of the three materials displaying essentially the same features and the following qualitative analysis is valid for all. At room temperature (dashed black line), the Ce L_3-edge spectrae exhibit two clear peaks, labelled A and B. Peak A is assigned to $Ce^{4+}$with the final state $2p4f^05d^1$, which denotes that an electron is excited from the 2p shell to the 5d shell, with no electron in the 4f shell. Peak B is also a Ce^{4+} peak, with the final state $2p4f^15d^1$v, which denotes that in addition to an electron excited from the Ce 2p shell to the 5d shell, another electron is also excited from the valence band (O 2p shell) to the Ce 4f shell, leaving a hole (v) in the valence band. The differences between the spectra collected at room temperature in air and at 500 °C in 21% O_2/N_2 (solid black line) are small. In reducing conditions at 500 °C (red and blue lines), it is possible to observe a decrease of the intensity of peak A, whereas peak B is deformed on the low energy range. This apparent modification of the peak shape is actually due to a new peak, labeled C, at slightly lower energy than the B peak. This peak is associated with the 4f occupancy in the initial state, and therefore is indicative of the presence of Ce^{3+} in the sample. In terms of the energy scale, the Ce L_3-absorption edges are close to 5725 eV in oxidizing conditions, while under reducing atmospheres they decrease to 5723 eV due to an increasing Ce^{+3} content.

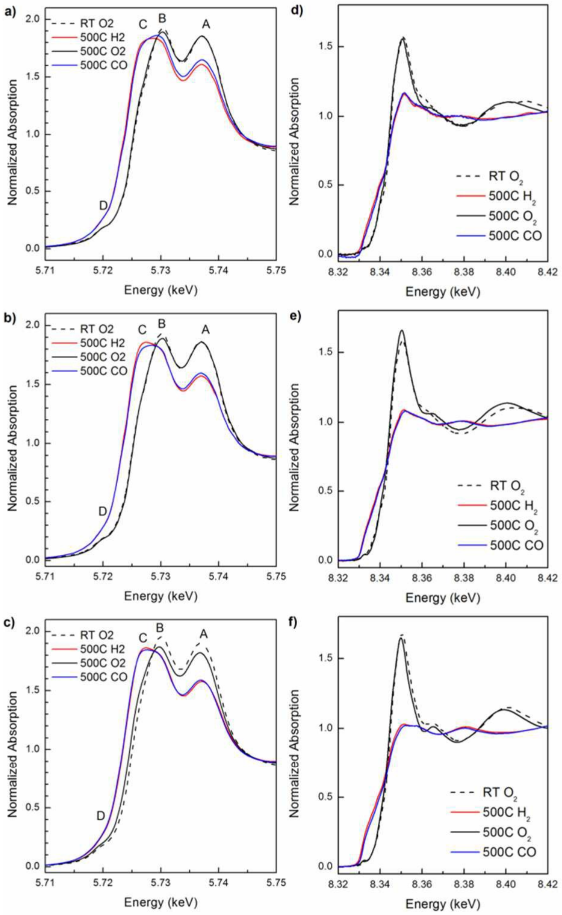

Figure 8. Normalized Ce L3-edge and Ni K-edge XANES spectra for (a,d) CeNi05, (b,e) CeNi10 and (c,f) CeNi20, respectively, obtained at room temperature (dashed line) and at 500 ºC in different subsequent atmospheres: 21% O_2/N_2 (black line), 5% H2/He (red line) and 5% CO/He (blue line).

Differences between oxidized and reduced samples are also apparent in the Ni K-edge XANES spectra plotted on **Figure 8 d, e and f** (using the same color code). Both spectra collected in air (dashed and solid black lines) exhibit the “white line” at ~8340 eV which can be assigned to the electronic transition from Ni $2p_{3/2}$ to the unoccupied 3d states, thus corresponding to octahedral coordinated Ni in +2 oxidation state. In reducing conditions (5% H_2/He and 5% CO/He, both at 500 °C), the intensity of this peak is strongly diminished and the onset of one additional small peak at ~8380 eV is apparent, both features suggesting the reduction of part of Ni^{+2} to Ni^{0}.[29] Note that the intensity of the latter peak increases with increasing nominal Ni content, in good quantitative agreement with the XRD patterns shown in **Figure 3**. On the other hand the white line is present in the spectra of the reduced samples, which means that Ni^{2+} is still present and forming the solid solution with ceria, (since XRD does not reveal the presence of NiO).

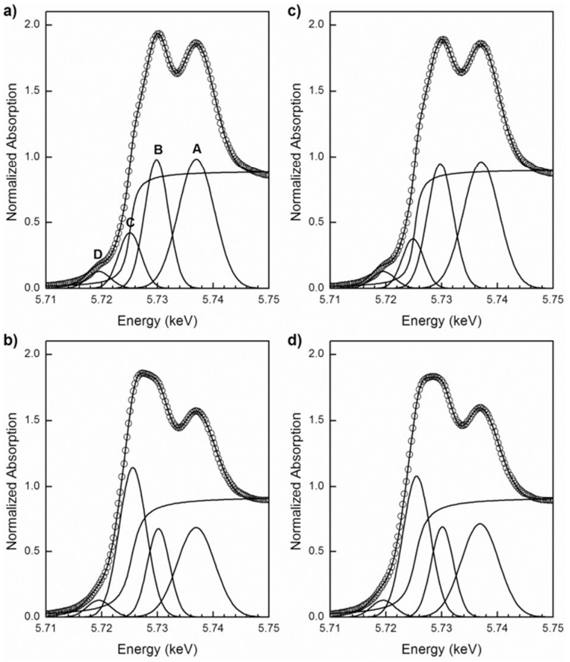

Figure 9. Normalized XANES spectra at the Ce L_3-edge for CeNi10 a) at room temperature in air and subsequently at 500 ºC under b) 5% H_2/He; c) 21% O_2/N_2 and d) 5% CO/He, showing the experimental data (empty circles), four Gaussian peaks (A–D), one arctangent function obtained by least-squares fitting and the sum of all five functions (continuous line).

In order to determine the fraction of Ce present as Ce^{3+}, data analysis was conducted by least-squares fitting 4 Gaussian profiles and 1 arctangent function to the experimental XANES spectra in the range between 5710 and 5750 eV. The 4 Gaussians are assigned to the already mentioned peaks A, B and C, plus one additional peak appearing at a ~5720 eV (labeled D) which is associated to both cationic species. The ratio between the area of peak C (due to Ce^{3+}) and the sum of the areas of peaks A, B and C (A and B due to Ce^{4+}) gives direct information about the fraction of Ce present as Ce^{3+}.[30] **Figure 9** shows examples of such fitting to the spectra of CeNi10 obtained in the usual variable experimental conditions (fittings to CeNi05 and CeNi20 data are shown in Supporting Information, **Figure S5** and **S6**). The increase in the area of peak C indicates that, under these reducing conditions, the amount of Ce present as Ce^{3+} at high temperature is larger than in the same sample under oxidizing conditions.

The results of these fits are shown in **Figure 10** normalized to a pure CeO_2 reference. The negative values observed for oxidizing conditions at room temperature (open circles) indicate that the sample contain a lower fraction of Ce^{3+} than this reference, but the differences are of the order of 2 or 3%, which is indeed very small. This finding is in good agreement with the room temperature XRD results collected in air, where the impact of Ni on the lattice parameters was also very small (Fig. 4, open circles) and the result of a trade-of between the smaller ionic radius of Ni2+ and the local lattice expansion due to the charge-compensating oxygen vacancies.

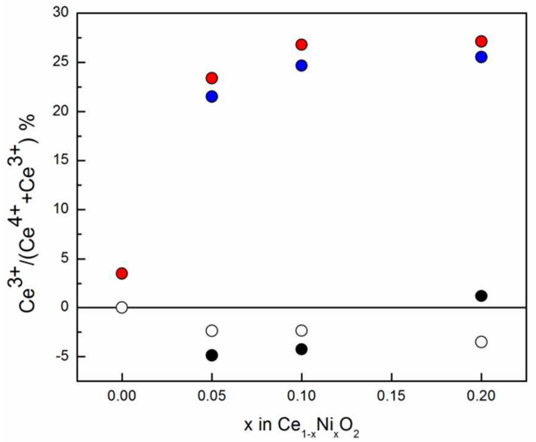

Figure 10. Fraction of Ce present as Ce^{3+}plotted as a function of the nominal Ni content in $Ce_{1-x}Ni_xO_{2-}$□ at obtained at room temperature (empty circles) and at 500ºC in atmospheres of 5% H_2/He (red circles), 21% O_2/N_2 (black circles) and 5% CO/He (blue circles).Values are calculated with respect to pure CeO_2. Negative values indicate that the sample contained a smaller percentage of Ce^{3+} than this reference.

The amount of Ce^{3+} increases on exposing the samples to 5%H_2/He, but with a huge effect of the presence of Ni. While for pure ceria this increase is negligible, in agreement with known phase diagrams,[3] the fraction of trivalent cerium reaches about 23% for CeNi05, and slightly increases for both CeNi10 and CeNi20, reaching a plateau at $Ce^{3+}/(Ce^{3+} + Ce^{4+})$=27%. This noticeable correlation between these data and the compositional dependence of the lattice parameters depicted in Figure 4 (red and blue circles) is a clear indication that the partial reduction of Ce^{4+} to Ce^{3+} is (and the concomitant generation of oxygen vacancies) is the most likely explanation for the further lattice expansion observed by SR-XRD at 500 °C in reducing atmospheres.

Reversing the atmosphere (still at 500 °C) to air fully reoxidizes the material, with the $Ce^{3+}/(Ce^{3+}+ Ce^{4+})$ ratio being similar to the initial room temperature values. Exposing the samples again to reducing conditions (5% CO/He) almost fully recovers the high Ce^{3+} fraction found for the 5%H_2/N_2 mixture, suggesting a good redox cycle ability of CeNi within these conditions. The slightly lower Ce^{3+} content in 5% CO/He than in 5% H_2/He can be explained by the slightly lower oxygen partial pressure expected for the hydrogen containing atmosphere.

The present set of results demonstrates that almost 10 at.% Ni^{2+} can be stabilized in the ceria lattice up to 500 °C under extremely reducing conditions, when the partial reduction of $Ce^{4+}$to the much larger Ce^{3+} is promoted. This effect, coupled to the generation of charge-balancing oxygen vacancies leads to the observed lattice expansion. The effect is the opposite of that observed for CeO_2 substituted with different lanthanides such as Gd (with fixed oxidation state +3), Pr and Tb (with oxidation states between +3 and +4), which tend to stabilize Ce^{4+}. In those cases a slight increase of the Ce^{3+} fraction is also observed, but this is typically of the order of 5% to 8% in terms of the $Ce^{3+}/(Ce^{3+} + Ce^{4+})$ ratio.[31-33]

Conclusions

In the present work, nanostructured $Ce_{1-x}Ni_xO_{2-y}$ (x = 0.5, 0.1, 0.15 and 0.2) powders were synthesized by a cation complexation method. All of the $Ce_{1-x}Ni_xO_{2-}$▯▯ samples were found to have a cubic crystal structure (Fm3m space group). Traces of segregated NiO phase were observed in as calcined samples with a Ni content higher than 15%. The nanopowders were composed of nanoparticles with an average crystallite size of about 5-7 nm. At room temperature, the lattice parameter of Ce-Ni mixed oxides increases when Ni content increases, probably due the formation of oxygen vacancies within ceria lattice. The same is observed at high temperature and reducing conditions. The solubility limit of Ni^{2+} in ceria is reduced to nearly 10 at.% Ni^{2+} at 500 °C in hydrogen atmosphere. In these conditions, and contrary to what is observed in pure ceria or the effect of other dopants such as Gd, Pr and Tb which tend to stabilize Ce^{4+}, up to 25% of the cerium cations are reduced to Ce^{3+}. Moreover, the Ce^{4+}/Ce^{3+} couple in nanocrystalline Ni-substituted ceria is highly reversible and it is this extraordinary redox ability associated to a high thermochemical stability of the material at relatively high temperature (at least up to 500 °C) and in strongly reducing conditions that provides the excellent catalytic properties for various very demanding processes and technological applications such as electrodes in SOFCs or gas separation membranes.

Acknowledgements

This work has been supported by: Science and Technological cooperation agreement MINCyT (Argentine) - MEC (Portugal), Project PO/14/04; the Brazilian Synchrotron Light Laboratory (LNLS, Brazil), under proposals D04B-XAFS1-17893 and D12A-XRD1-17860; Agencia Nacional de Promoción Científica y Tecnológica (Argentina, PICT 2012-1506); and by the Portuguese Foundation for Science and Technology (FCT) through projects CICECO-Aveiro Institute of Materials (FCTUID/CTM/50011/2013), financed by national funds through the FCT/MEC, and when applicable, co-financed by FEDER under the PT2020 Partnership Agreement, and Investigador FCT 2013 contract number IF/01174/2013.The authors are grateful to Anna Paula da Silva Sotero Levinsky, Cristiane Rodella, Fábio Zambello, Tamiris Bouças Piva and Simone Baú Betim for their invaluable experimental assistance at the LNLS. Dr. L.M. Acuña and Dr. R.O. Fuentes are members of CIC-CONICET, Argentina.

Notes and references

1 J. Kaspar and P. Fornasiero, *Catalysis by Ceria and Related Materials*; Trovarelli, A., Ed.; Imperial College Press: London, 2002 Ch. 6.

2 R. Di Monte and J. Kaspar, On the role of oxygen storage in three-way catalysis. *Top. Catal*. 2004, **28**, 47-57.

3 M. Mogensen, N. M. Sammes, G. A. Tompsett, Physical, chemical and electrochemical properties of pure and doped ceria. *Solid State Ionics* 2000, **129**, 63.

4 W. C. Chueh, Y. Hao, W. Jung and S. M. Haile, High electrochemical activity of the oxide phase in model ceria-Pt and ceria-Ni composite anodes. *Nat. Mater.* 2012, **11**, 155.

5 Y. Zhang and M. Flytzani-Stephanopoulos, Hydrothermal stability of cerium modified Cu-ZSM-5 catalyst for nitric oxide decomposition. *J. Catal.* 1995, **153**, 317.

6 Q. Fu, H. Saltsburg and M. Flytzani-Stephanopoulos, Active nonmetallic Au and Pt species on ceria-based water-gas shift catalysts. *Science* 2003, **301**, 935.

7 Y. Liu, T. Hayakawa, K. Suzuki, S. Hamakawa, T. Tsunoda, T. Ishii and M. Kumagai, Highly active copper/ceria catalysts for steam reforming of methanol. *Appl. Catal., A,* 2002, **223**, 137.

8 X. Wang, M. Shen, J. Wang and S. Fabris, Enhanced oxygen buffering by substitutional and interstitial Ni point defects in ceria: A first-principles DFT+U study. *J. Phys. Chem. C* 2010, **114**, 10221–10228.

9 Y. Wang, A. Zhu, Y. Zhang, C. T. Au, X. Yang and C. Shi, Catalytic reduction of NO by CO over NiO/CeO2 catalyst in stoichiometric NO/CO and NO/CO/O2 reaction. *Appl. Catal., B,* 2008, **81**, 141–149.

10 M. M. Pakulska, C. M. Grgicak and J. B. Giorgi, The effect of metal and support particle size on NiO/CeO2 and NiO/ZrO2 catalyst activity in complete methane oxidation. *Appl. Catal., A* 2007, **332**, 124–129.

11 S. Xu, X. Yan and X. Wang, Catalytic performances of NiO-CeO2 for the reforming of methane with CO2 and O2. *Fuel* 2006, 85, 2243–2247.

12 Z. Tao, G. Hou, N. Xu and Q. Zhang, A highly coking-resistant solid oxide fuel cell with a nickel doped ceria: Ce1-xNixO2-y reformation layer. *Int. J. Hydrogen Energy* 2014, **39**, 5113-5120.

13 A. Thurber, K.M. Reddy, V. Shutthanandan, M.H. Engelhard, C. Wang, J. Hays and A. Punnoose, Ferromagnetism in chemically synthesized Ce O2 nanoparticles by Ni doping. *Phys. Rev. B* 2007, **76**, 165206.

14 J. C. Bear, P. D. McNaughter, P. Southern, P. O'Brien and C. W. Dunnill, Nickel-doped ceria nanoparticles: The effect of annealing on room temperature ferromagnetism. *Crystals* 2015, **5**, 312-326.

15 A. Bouaine, R. J. Green, S. Colis, P. Bazylewski, G. S. Chang, A. Moewes, E. Z. Kurmaev and A. Dinia, Appearance of ferromagnetism in co-doped CeO2 diluted magnetic semiconductors prepared by solid-state reaction. *J. Phys. Chem. C* 2011, **115**, 1556-1560

16 J. A. Rodriguez, X. Wang, J. C. Hanson, G. Liu, A. Iglesias-Juez and M. Fernandez-Garcia, The behavior of mixed-metal oxides: Structural and electronic properties of $Ce_{1-x}Ca_xO_2$ and $Ce_{1-x}Ca_xO_{2-x}$. *J. Chem. Phys.* 2003, **119**, 5659.

17 R. D. Shannon, Revised effective ionic radii and systematic studies of interatomic distances in halides and chalcogenides. *Acta Cryst*. 1976, **A32**, 751-767.

18 L. Barrio, A. Kubacka, G. Zhou, M. Estrella, A. Martínez-Arias, J. C. Hanson, M. Fernández-García and J. A. Rodriguez, Unusual physical and chemical properties of ni in Ce1- xNi xO2-y oxides: Structural characterization and catalytic activity for the water gas shift reaction. *J. Phys. Chem. C,* 2010, 114, **29**, 12689-12697.

19 R. O. Fuentes and R. T. Baker, Synthesis and properties of gadolinium-doped ceria solid solutions for IT-SOFC electrolytes. *Int. J. Hydrogen Energy* 2008, **33**, 3080-3084.

20 J. Rodríguez-Carvajal, FullProf Suite Program, Version 2.05. Laboratoire León Brillouin. Saclay, France: CEA-CNRS; 2011

21 R. A. Young, in: R. A. Young (Ed), TheRietveld Method, Oxford University Press, Oxford, 1993, Chapter 1, pp. 21-24.

22 H. Klug and L. Alexander, in: X-ray Diffraction Procedures for Polycrystalline and Amorphous Materials, John Wiley, New York, 1974, p. 618.

23 R. A. Rocha and E. N. S. Muccillo, Physical and chemical properties of nanosized powders of gadolinia-doped Ceria prepared by the cation complexation technique. *Materials Research Bulletin* 2003, **38**, 15, 1979–1986.

24 R. O. Fuentes and R. T. Baker, Structural, morphological and electric properties of $Gd_{0.1}Ce_{0.9}O_{1.95}$prepared by a citrate complexation method. *J. Power Sources* 2009, **186** 2, 268-277.

25 R. O. Fuentes, D. J. Woollins and R. T. Baker, Temperature effects on structural properties in the synthesis of nanocrystalline $Zr_{0.5}Ce_{0.5}O_2$ solid solution: A study by XRD and HRTEM. *J. Alloys Compounds* 2010,**495**, 565-569.

26 S. Tsunekawa, K. Ishikawa, Z.-Q. Li, Y. Kawazoe, A. Kasuya, Erratum: Origin of anomalous lattice expansion in oxide nanoparticles (Physical Review Letters, 2000, 85, 3440). *Phys. Rev. Lett.* 2002 **85**, 3440.

27 X.-D. Zhou and W. Huebner, Size-induced lattice relaxation in CeO_2 nanoparticles. *Applied Physics Letters* **79**, 3512-3514

28 H. Hayashi, M. Kanoh, C. J. Quan, H. Inaba, S. Wang, M. Dokiya and H. Tagawa, Thermal expansion of Gd-doped ceria and reduced ceria. *Solid State Ionics* 2000, **132**, 227–233

29 A. M. Beale, M. Paul, G. Sankar, R. J. Oldman, C. R. A. Catlow, S. French and M. Fowles, Combined experimental and computational modelling studies of the solubility of nickel in strontium titanate. *J. Mater. Chem.* 2009, **19**, 4391–4400.

30 F. Zhang, P. Wang, J. Koberstein, S. Khalid and S-W. Chan, Cerium oxidation state in ceria nanoparticles studied with X-ray photoelectron spectroscopy and absorption near edge spectroscopy. *Surf. Sci.* 2004, **563**, 74-82.

31 F. F. Muñoz, R. T. Baker, A. G. Leyva and R.O. Fuentes, Reduction and catalytic behaviour of nanostructured Pd/gadolinia-doped ceria catalysts for methane combustion. *Appl. Catal. B: Environmental* 2013, **136-137**, 122-132.

32 F. F. Muñoz, L. M. Acuña, C. Albornoz, A. G. Leyva, R. T. Baker and R.O. Fuentes, Redox properties of nanostructured lanthanide-doped ceria spheres prepared by microwave assisted hydrothermal homogeneous co-precipitation. *Nanoscale* 2015, **7**, 271-181.

33 L. M. Acuña, F. F. Muñoz, C. Albornoz, A. G. Leyva, R. T. Baker and R.O. Fuentes, Nanostructured terbium-doped ceria spheres: Effect of dopant on physical and chemical properties under reducing/oxidizing conditions. *J. Mater. Chem. A* 2015, **3**, 16120-16131.

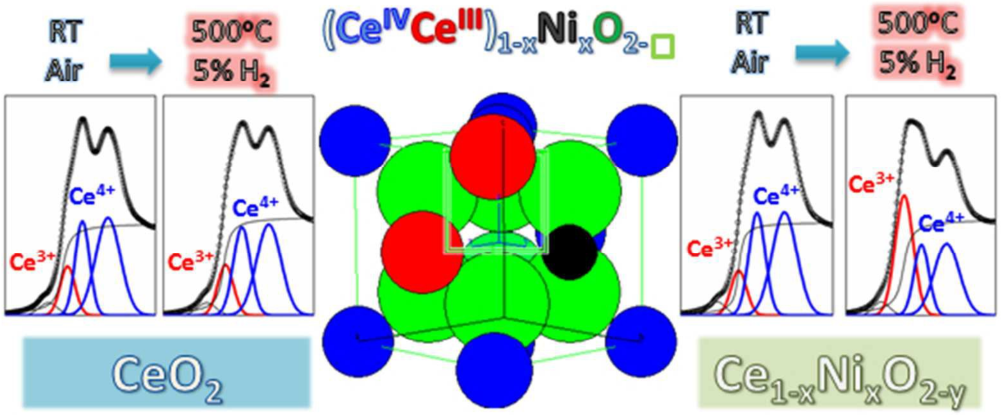

The Ce4+/Ce3+ couple in nanocrystalline Ni-doped ceria is highly reversible and its extraordinary redox cyclicality associated to a high thermochemical stability of the material at relatively high temperature (500 °C)

155x67mm (96 x 96 DPI)